

Revolutionary High-entropy Zr-Y-Yb-Ta-Nb-O Oxides for Next Generation Thermal Barrier Coating Applications

Yao Yao

Shanghai Jiao Tong University

Fan Yang

Shanghai Jiao Tong University

Xiaofeng Zhao (✉ xiaofengzhao@sjtu.edu.cn)

Shanghai Jiao Tong University

Ping Xiao

Shanghai Jiao Tong University

Article

Keywords: Thermal barrier coating, High entropy, Toughness, Thermal conductivity.

Posted Date: February 2nd, 2021

DOI: <https://doi.org/10.21203/rs.3.rs-152197/v1>

License:  This work is licensed under a Creative Commons Attribution 4.0 International License.

[Read Full License](#)

Revolutionary High-entropy Zr-Y-Yb-Ta-Nb-O Oxides for Next Generation Thermal Barrier Coating Applications

Yao Yao ^a, Fan Yang ^b, Xiaofeng Zhao ^{a,*}, Ping Xiao ^a

^a Shanghai Key Laboratory of High Temperature Materials and Precision Forming, Shanghai Jiao Tong University, 800 Dongchuan Road, Shanghai 200240, China

^b School of Mechanical Engineering, Shanghai Jiao Tong University, 800 Dongchuan Road, Shanghai 200240, China

Abstract

We report a revolutionary ceramic material with exceptional high temperature stability and superior thermo-mechanical properties for next generation thermal barrier coatings (TBCs) for aeroengines. The multicomponent oxides ($Zr_{1-4x}Y_xYb_xTa_xNb_xO_2$) designed via a high entropy concept could exhibit a double tetragonal phase. The optimized composition breaks the limitation of intrinsic brittleness in previously reported TBC candidate materials and shows a superior toughness up to $\sim 4.59 \text{ MPa m}^{1/2}$ due to ferroelastic and phase transformation toughening mechanisms. It also shows a remarkable high temperature stability at 1600 °C, which is almost 400 °C higher than the state-of-the-art yttria stabilized zirconia TBC material. In addition, it also exhibits a significantly lower thermal conductivity ($\sim 1.37 \text{ W}\cdot\text{m}^{-1}\cdot\text{K}^{-1}$ at 900 °C) and a higher coefficient of thermal expansion ($\sim 11.3 \times 10^{-6} \text{ K}^{-1}$ at 1000 °C), as well as excellent corrosion resistance to molten silicate ($\sim 2.9 \text{ }\mu\text{m/h}$ at 1300 °C). This work provides a new approach to design ceramics by extending the high-entropy concept to both medium-entropy and high-entropy compositions searching for multifunctional properties.

Keywords: Thermal barrier coating; High entropy; Toughness; Thermal conductivity.

* Corresponding author: Xiaofeng Zhao, E-mail: xiaofengzhao@sjtu.edu.cn.

1. Introduction

Thermal barrier coatings (TBCs) are widely employed to protect the metallic components of gas turbine engines from direct exposure to high-temperature gas stream [1-3]. In the pursuit of enhanced engine efficiency, there has been an ever-increasing demand for increasing the operation temperature of engines. The state-of-the-art TBCs material, 7-8 wt.% yttria stabilized zirconia (7-8YSZ), is approaching its temperature limit, due to the destructive tetragonal to monoclinic (t-m) phase transformation when temperature exceeds 1200 °C [4], and the devastating corrosion from the low-melting-point oxides CaO-MgO-Al₂O₃-SiO₂ (CMAS) from sand, volcano ash and dust at elevated temperatures [5]. Driven by the urgent demand of next-generation TBCs materials working at > 1200 °C, numerous efforts have been devoted to developing novel ceramics to replace YSZ. To work at higher temperatures, such materials have to meet a number of strict criteria including low thermal conductivity, outstanding high-temperature phase stability, high coefficient of thermal expansion (CTE), good chemical compatibility with thermally grown oxide (TGO), high resistance to CMAS corrosion and excellent mechanical properties. Although many new materials such as rare earth zirconates (RE₂Zr₂O₇) [6], LaMgAl₁₁O₁₉ [7] and perovskites [8] have been proposed, none of them can satisfy all the above property requirements. Developing next generation TBCs materials remains a big challenge.

Recently, multicomponent high-entropy engineering offers a new approach to design high performance materials. High entropy materials usually have high lattice strain and thereby exhibit a low thermal conductivity, a high hardness, and other promising properties [9-12]. Tailoring the composition, defects, and degree of disorder of materials, high-entropy engineering provides a possible approach to achieve better and more tunable properties for TBCs applications. For instance, Lu *et al.* [11] designed a type of Y/Hf-doped AlCoCrFeNi high-entropy alloys (HEAs) with superior oxidation and spallation resistance, which are promising to replace the conventional NiCoCrAlY bond coat for TBCs. For high-entropy oxides (HEOs) as top coat for TBCs, Ren *et al.* [12] fabricated a multicomponent high-entropy rare earth zirconate (5RE₂Zr₂O₇), which

shows a larger coefficient of thermal expansion ($\sim 11 \times 10^{-6} \text{ K}^{-1}$, 1273 K) and a lower thermal conductivity ($0.86 \text{ W m}^{-1} \text{ K}^{-1}$, 1273 K) than the monolithic $\text{RE}_2\text{Zr}_2\text{O}_5$. However, the fracture toughness ($\sim 2.24 \text{ MPa m}^{1/2}$) of $5\text{RE}_2\text{Zr}_2\text{O}_7$ is too low to meet the requirement for TBCs. Nevertheless, HEOs show great potential as TBCs top coat materials, which motivates the search and development of novel HEOs with desired properties, in particular, high fracture toughness in addition to high-temperature stability, low thermal conductivity and high CTE.

Among the known candidate materials, the $\text{ZrO}_2\text{-YO}_{1.5}\text{-TaO}_{2.5}$ (ZYTO) system shows promising properties for TBC applications. ZYTO oxides with equimolar $\text{YO}_{1.5}$ and $\text{TaO}_{2.5}$ demonstrate low and temperature-independent thermal conductivities ($1.4\sim 2.0 \text{ W}\cdot\text{m}^{-1}\cdot\text{K}^{-1}$) owing to a minimum phonon mean free path [13], and meanwhile exhibit adequate toughness due to the ferroelastic transformation similar to 7-8YSZ [14]. However, the stable tetragonal region in the $\text{ZrO}_2\text{-YO}_{1.5}\text{-TaO}_{2.5}$ phase diagram is extremely narrow [15], as a consequence, the composition and phase may easily deviate from its original state after high temperature operation, which significantly restricts their applicability in TBCs. This fatal problem may be solved by high entropy engineering as a large number of equivalent sites in a crystal with an intermediate sublattice will increase the configurational entropy and expand the elemental diversity containable in a single solid solution [16-18].

Here we aim to design a high-performance top coat material for TBCs used in next generation aeroengines via the high entropy strategy. We propose multicomponent HEOs based on ZYTO, in which equal-molar Yb and Nb are introduced to partially substitute Y and Ta, respectively. The multicomponent high entropy $\text{Zr}_{1-4x}\text{Y}_x\text{Yb}_x\text{Ta}_x\text{Nb}_x\text{O}_2$ tetragonal oxides exhibit significantly improved properties than the previously reported TBC candidate materials. The optimized composition shows a superior high temperature stability up to 1600 °C, a high fracture toughness of $\sim 4.59 \text{ MPa m}^{1/2}$, a low thermal conductivity of $\sim 1.37 \text{ W}\cdot\text{m}^{-1}\cdot\text{K}^{-1}$ at 900 °C, a high CTE of $\sim 11.3 \times 10^{-6} \text{ K}^{-1}$ at 1000 °C, as well as an excellent corrosion resistance to CMAS ($\sim 2.9 \mu\text{m h}^{-1}$ at 1300 °C). Such revolutionary top coat materials are expected to facilitate the

development of next-generation aeroengines working at higher temperatures with significantly enhanced efficiency.

2. Results

Microstructure and phase composition. $Zr_{1-4x}Y_xYb_xTa_xNb_xO_2$ ($x = 0.2, 0.172, 0.142, 0.114$ and 0.083) oxides were prepared by solid-state reaction followed by free-sintering (details are given in *Methods* Section in Supplementary Information). The composition dependence of configurational entropy (ΔS) was determined by $\Delta S = -k_B \sum_{i=1}^N x_i \log(x_i)$ [9], where x_i is the atom fraction of element i and k_B is the Boltzmann constant. t-1 ($x = 0.2$) and t-2 ($x = 0.172$) samples with $> 1.5k_B$ per cation ideal mixing configurational entropy were defined as high-entropy ceramics, and t-3 to t-5 samples with mixing configurational entropy in the range of $1-1.5k_B$ per cation were defined as medium-entropy ceramics (Table S1) [18]. $(Zr_{0.2}Hf_{0.2}Y_{0.2})Gd_{0.2}La_{0.2}O_2$ and $(Zr_{0.2}Hf_{0.2}Y_{0.2})Gd_{0.2}Nd_{0.2}O_2$ HEOs with cubic fluorite structure (*c*-HEO) were also prepared by the same method for comparison.

Phase compositions of $Zr_{1-4x}Y_xYb_xTa_xNb_xO_2$ oxides and *c*-HEOs were identified by X-ray diffraction patterns (Fig. 1a and 1b). The equimolar composition ($x = 0.2$, labelled as t-1) presents a single monoclinic structure (M- $ABO_4(ZrO_2)$), suggesting incorporation of ZrO_2 into the ABO_4 solid solution, where site A in the crystal structure ABO_4 represents Y/Yb and B represents Ta/Nb. The phase composition of t-1 sample is further examined by EDS elemental mapping (Fig.S1a), where a ZrO_2 -rich phase can be observed. In combination of XRD and EDS results, it is concluded t-1 consists of M- $ABO_4(ZrO_2)$ with small amount of ZrO_2 -rich particles. The t-2 sample ($x = 0.172$) with higher ZrO_2 content (31.2 mol %) shows a single tetragonal phase (T- $ABO_4(ZrO_2)$), which is supported by the homogeneous elemental distribution revealed by EDS (Fig.S1b). It is worth mentioning that the composition $Zr_{0.312}Y_{0.344}Ta_{0.344}O_2$ with same ZrO_2 content in the ZYTO system is a mixed monoclinic and tetragonal phase [19]. Therefore, the single T- $ABO_4(ZrO_2)$ phase in t-2 suggests an enhanced phase stability

induced by high-entropy effects [20]. On the other hand, the enhanced Zr^{4+} content from 20 mol % in t-1 to 31.2 mol % in t-2 decreases the monoclinic (M) \rightarrow tetragonal (T) phase transformation temperature in ABO_4 [21], which may also contribute to retaining the single T- $ABO_4(ZrO_2)$ in t-2. Further decrease in x to 0.142 (t-3) and 0.114 (t-4) results in a double tetragonal structure (T- $ABO_4(ZrO_2)$ + t- $ZrO_2(ABO_4)$), which can be clearly identified by XRD (Fig.1a and 1b), EDS mapping and BSE observation (Fig.S1c and 1d). Furthermore, t-4 shows a higher peak intensity of t- $ZrO_2(ABO_4)$ than t-3 (Fig.1b), which agrees with the increased amount of the Zr-rich phase observed by EDS mapping and BSE images in Fig.S1c and d. Formation of the two-phase structure results from the limited solubility of ZrO_2 in the T- ABO_4 solid solution. Furthermore, a high mixing configuration entropy, associated with mass difference, lattice distortion, and chemical bonding deviation, may cooperatively promote the formation of simple compounds with multiphase elements [22]. For $x = 0.083$ (t-5) corresponding to a Zr concentration of 66.8 mol %, the sample displays a single tetragonal phase (t- $ZrO_2(ABO_4)$), as revealed by XRD (Fig.1a and 1b) and EDS mapping (Fig.S1e). To sum the above, with decreasing x in $Zr_{1-4x}Y_xYb_xTa_xNb_xO_2$ (increasing Zr concentration), the high-entropy oxide experiences a structure change from M- $ABO_4(ZrO_2)$, T- $ABO_4(ZrO_2)$, T- $ABO_4(ZrO_2)$ + t- $ZrO_2(ABO_4)$ to t- $ZrO_2(ABO_4)$.

SEM observation of the thermal-etched t-4 sample shows the two tetragonal phases, t- $ZrO_2(ABO_4)$ and T- $ABO_4(ZrO_2)$, can coexist in the same grain, as marked by the dashed circle region in Fig.1c, where the darker phase represents the ZrO_2 enriched tetragonal phase (t- $ZrO_2(ABO_4)$) due to its lower mean atomic number. High-angle annular dark-field (HAADF) image by atomic-resolution scanning transmission electron microscopy (STEM) (Fig.1d) reveals a low angle lattice misfit between t- $ZrO_2(ABO_4)$ and T- $ABO_4(ZrO_2)$ phase without any obvious lattice defect near or at the interphase boundary. The lattice is continuous across the interphase boundary and the (101) lattice spacing is ~ 0.301 nm in the T- $ABO_4(ZrO_2)$ phase and 0.297nm in the t- $ZrO_2(ABO_4)$ phase.

Fig.1e illustrates the atomic arrangements in a unit cell of T- $ABO_4(ZrO_2)$ and t-

$\text{ZrO}_2(\text{ABO}_4)$. The crystal structure of $\text{T-ABO}_4(\text{ZrO}_2)$ (space group 141, $I4_1/amd$) is derived from the high-temperature tetragonal YTaO_4 phase [23]. Zr^{4+} ions are most likely to equally replace the neighboring A^{3+} and B^{4+} sites to preserve charge neutrality and to adopt a stable four-fold coordination for Zr^{4+} in the T-ABO_4 structure. For the $\text{t-ZrO}_2(\text{ABO}_4)$ solid solution (space group 137, $P4_2/nmc$), the tetragonal ABO_4 phase is rotated by 45° about the common c-axis and the volume of the tetragonal ZrO_2 phase unit cell is approximately four times the volume of a tetragonal ABO_4 phase unit cell [19]. The tetragonal structure of $\text{T-ABO}_4(\text{ZrO}_2)$ can be retained at room temperature as revealed by the reflections in the $[\bar{1}11]_{\text{ZAP}}$ (Fig.1f). Meanwhile, the $\{112\}$ reflections in Fig.1g confirm single $\text{t-ZrO}_2(\text{ABO}_4)$ structure. In both tetragonal phases, identical long-range ordered atomic arrangements are formed during alloying in view of the larger solubility ranges and the equal trade-off between two Zr^{4+} and one $\text{A}^{3+}\text{B}^{5+}$ group. Notably, the complex co-doping at A and B sites of ABO_4 structure results in short-range disordered atomic arrangements and thus increases the configuration entropy, along with mass difference and local lattice distortion.

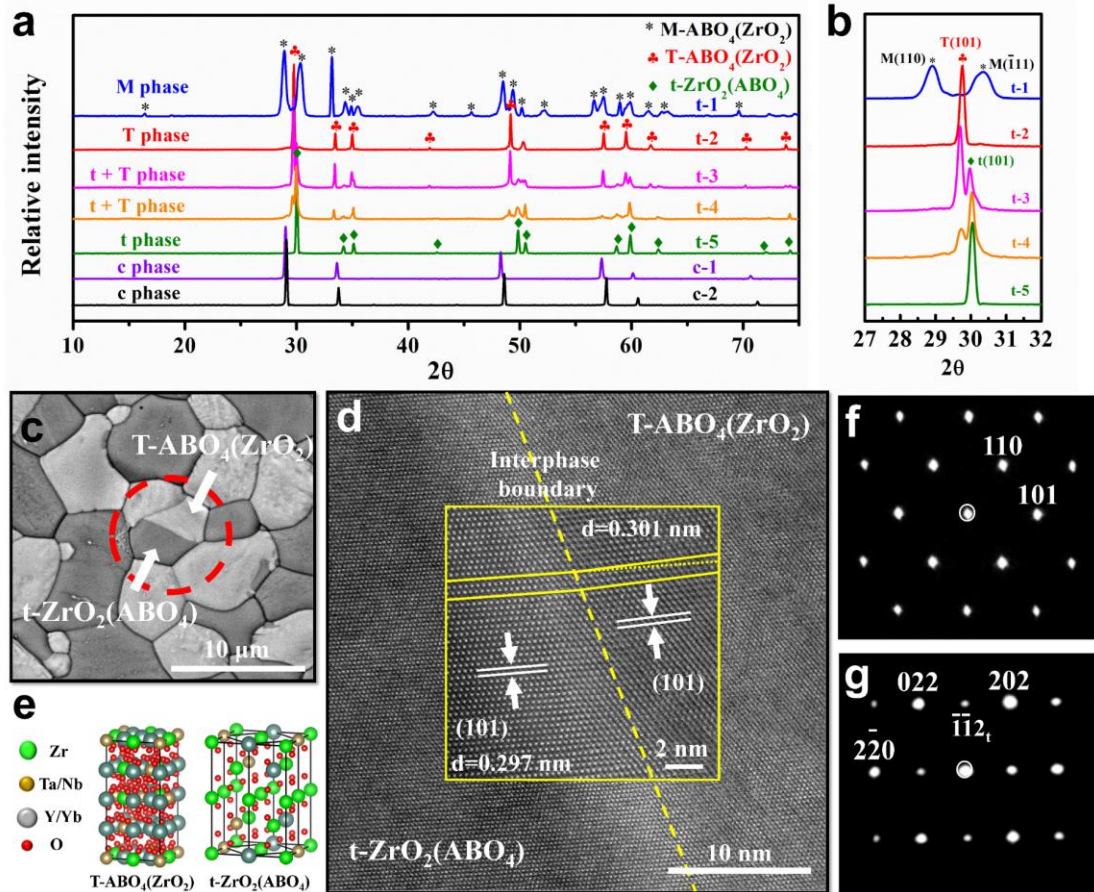


Figure. 1 | Phase identification. (a) XRD patterns of $Zr_{1-4x}Y_xYb_xTa_xNb_xO_2$ oxides and cubic phase HEOs (site A in the crystal structure ABO_4 represents Y or Yb, and site B represents Ta or Nb); (b) Slow scan ($0.5^\circ \text{ min}^{-1}$) of the 2θ range between 27° and 32° to distinguish the monoclinic and tetragonal phase; (c) BSE image of the grain with the double tetragonal phases in the t-4 sample; (d) Atomic-resolution HAADF STEM image of the interphase boundary between the $T-ABO_4(ZrO_2)$ and $t-ZrO_2(ABO_4)$ phase (the inset figure is an expanded view of the interphase boundary); (e) Crystal structure of $T-ABO_4(ZrO_2)$ and $t-ZrO_2(ABO_4)$ created using VESTA software package; (f) The $[111]_{ZAP}$ of $T-ABO_4(ZrO_2)$ and (g) the $[111]_{ZAP}$ of $t-ZrO_2(ABO_4)$.

Thermal properties and CMAS resistance. Fig.2a shows the thermal conductivities of $Zr_{1-4x}Y_xYb_xTa_xNb_xO_2$ oxides between 200 and 900 °C together with those for 8YSZ [24], ZYTO oxides [13] and the *c*-HEOs for comparison. $Zr_{1-4x}Y_xYb_xTa_xNb_xO_2$ oxides show almost temperature-independent thermal conductivities despite of a noticeable

increase of thermal conductivity at $T > 600$ °C for t-1 and t-5, which may be related to a thermal radiation effect. Why radiation effect is significant only in t-1 and t-5 remains unclear at the moment and needs further investigation. Nevertheless, $Zr_{1-4x}Y_xYb_xTa_xNb_xO_2$ oxides exhibit much lower thermal conductivities ($1.37\sim 1.84$ $W\cdot m^{-1}\cdot K^{-1}$ at 900 °C) than 8YSZ (> 2.5 $W\cdot m^{-1}\cdot K^{-1}$). Among all the compositions, t-4 shows the lowest thermal conductivity (~ 1.37 $W\cdot m^{-1}\cdot K^{-1}$) at 900 °C, which is also significantly lower than ZYTO at the same temperature [13]. In Fig.2a, c-HEOs display the lowest thermal conductivity (~ 0.83 $W\cdot m^{-1}\cdot K^{-1}$) due to the increased phonon scattering from mass difference and bond disorder. Point defects and oxygen vacancies in the cubic fluorite structure of c-HEOs also contribute to reduce thermal conductivity. Unlike the c-HEOs and 8YSZ, $Zr_{1-4x}Y_xYb_xTa_xNb_xO_2$ oxides do not contain any oxygen vacancy. The low thermal conductivities of $Zr_{1-4x}Y_xYb_xTa_xNb_xO_2$ oxides can be described by a point defects scattering model reported in the ZYTO system [13]. Furthermore, incorporation of Zr into both A and B sites of the ABO_4 structure of ZYTO increases the configurational entropy, induces higher mass disorder and shortens the phonon mean free path, resulting in a further reduction of the thermal conductivity of ZYTO.

Apart from thermal conductivity, CTE is also a critical criterion for top coat material. A large CTE is required to minimize the thermal mismatch stress between the top coat and the metallic bond coat [1]. Fig.2b plots the CTE of $Zr_{1-4x}Y_xYb_xTa_xNb_xO_2$ oxides measured from room temperature to 1400 °C. t-4 sample displays the highest CTE ($\sim 11.3 \times 10^{-6}$ K^{-1} , 1000 °C) among the $Zr_{1-4x}Y_xYb_xTa_xNb_xO_2$ oxides, which is higher than YSZ ($\sim 10.5 \times 10^{-6}$ K^{-1} , 1000 °C) [5] and c-HEOs. High-entropy composition t-2 with single T- ABO_4 (ZrO_2) solid solution shows the lowest CTE ($\sim 9.01 \times 10^{-6}$ K^{-1} , 1000 °C), and the CTE increased significantly with the increasing of t- ZrO_2 (ABO_4) phase contents from t-2 to t-4. It should be noted that t-4 presents a higher CTE than t-5 with a single t- ZrO_2 (ABO_4) phase. This may be attributed to the higher Zr^{4+} content in the t- ZrO_2 (ABO_4) phase in t-4 (~ 73.7 mol.%) than that in t-5 (~ 66.8 mol.%) as later revealed by EDS mapping. The enhanced tetragonality [21] and anisotropic expansion of t- ZrO_2 (ABO_4) contribute to the higher CTE in t-4.

Compared with YSZ and other attractive oxides for TBCs, such as aluminates [7], pyrochlores [25], $\text{RE}_2\text{Sn}_2\text{O}_7$ [26], RETaO_4 [27], and $3\sim 5\text{RE}_2\text{Zr}_2\text{O}_7$ [12], the multicomponent medium- and high-entropy $\text{Zr}_{1-4x}\text{Y}_x\text{Yb}_x\text{Ta}_x\text{Nb}_x\text{O}_2$ tetragonal oxides show competitive low thermal conductivity and large CTE as promising TBC material (Fig. 2c).

Serving under long-term extreme high-temperature conditions, TBC materials should have preeminent high-temperature phase stability to avoid the catastrophic damage from phase transformation. However, most HEOs undergo a segregation of second phase after long-term high-temperature heat treatment [28]. To evaluate the long-term thermal phase stability of $\text{Zr}_{1-4x}\text{Y}_x\text{Yb}_x\text{Ta}_x\text{Nb}_x\text{O}_2$ oxides, they are subjected to heat treatment at 1600 °C for 100 h. XRD patterns (Fig.S3) show absence of any second phase or phase transformation of $\text{Zr}_{1-4x}\text{Y}_x\text{Yb}_x\text{Ta}_x\text{Nb}_x\text{O}_2$ oxides (except for t-5) after exposure to 1600 °C for 100 h, indicating the excellent high-temperature phase stability of these oxides. In particular, the t-4 sample with coherent double tetragonal phases is prone to form a single tetragonal phase after long-term heat treatment (Fig.2d), which suggests the development of an enhanced high-temperature phase stability.

As t-4 presents the lowest thermal conductivity, highest CTE and exceptional high-temperature stability, its resistance against CMAS corrosion is evaluated and compared with those of the state-of-the-art YSZ and the excellent CMAS-resistant material $\text{Gd}_2\text{Zr}_2\text{O}_7$ [29], as shown in Fig.2e. At 1300 °C, the total infiltration depth in t-4 shows a rapid increase ($\sim 26 \mu\text{m}$) after 1 h CMAS corrosion, and then increases to $\sim 144 \mu\text{m}$ after 50 h with a slow infiltration rate of $\sim 2.9 \mu\text{m h}^{-1}$, which is comparable to the superior CMAS resistance performance of $\text{Gd}_2\text{Zr}_2\text{O}_7$ ($\sim 2.7 \mu\text{m h}^{-1}$). Cross-sectional SEM images of t-4 after CMAS corrosion at 1300 °C for 1-50 h show the formation of a uniform CMAS infiltration layer (Fig.S4). The soluble product slightly precipitates from the CMAS melt with increasing corrosion time and the CMAS melt still exists after 50 h corrosion, suggesting a slow dissolution and precipitation rate of t-4 in the CMAS melt. Thus, it can be concluded that t-4 has an excellent resistance to CMAS corrosion at 1300 °C.

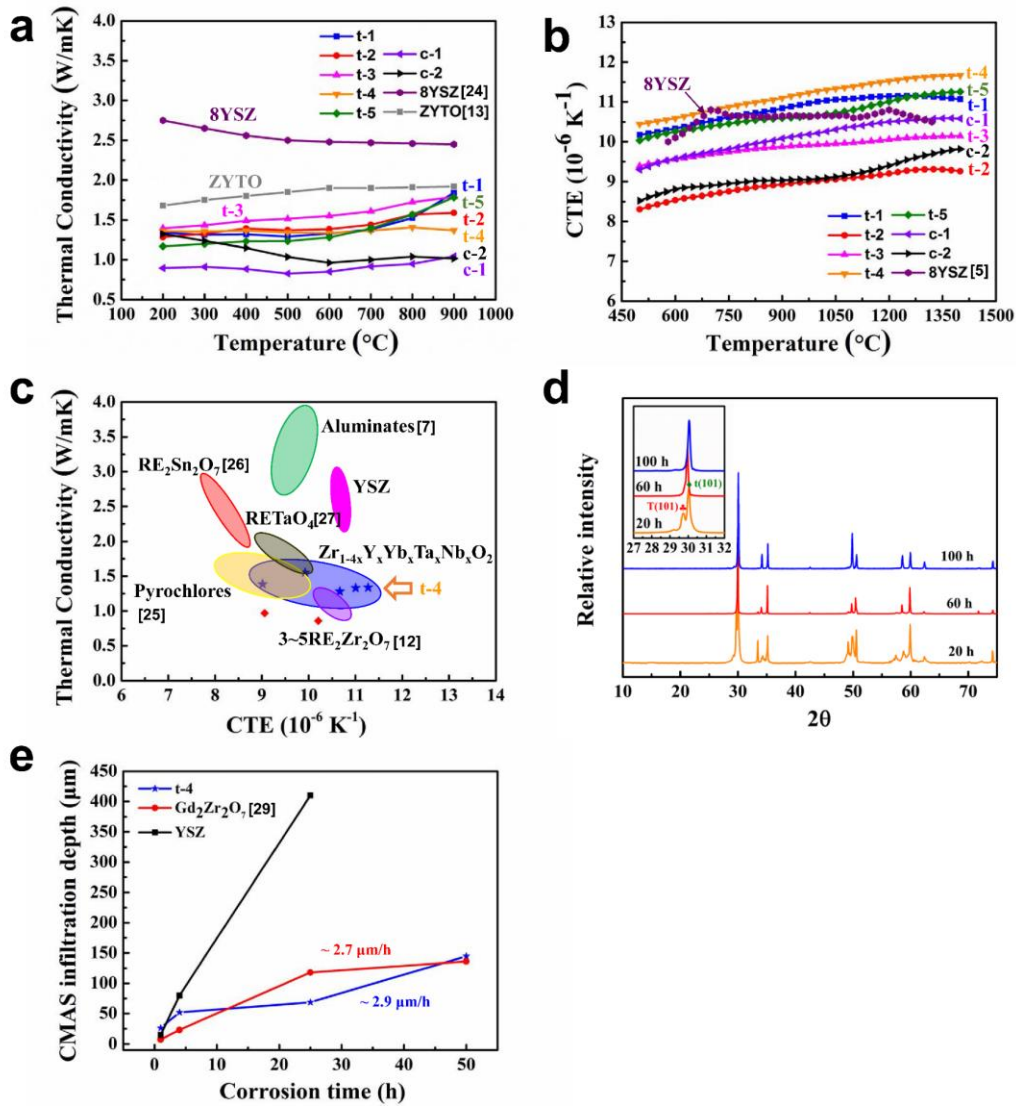


Figure. 2 | Thermal properties and CMAS resistance. (a) Thermal conductivity of $\text{Zr}_{1-4x}\text{Y}_x\text{Yb}_x\text{Ta}_x\text{Nb}_x\text{O}_2$ oxides, compared with YSZ and ZYTO; (b) Thermal expansion coefficient of $\text{Zr}_{1-4x}\text{Y}_x\text{Yb}_x\text{Ta}_x\text{Nb}_x\text{O}_2$ oxides, compared with YSZ; (c) Thermal conductivity as a function of thermal expansion coefficient (the blue points are data of $\text{Zr}_{1-4x}\text{Y}_x\text{Yb}_x\text{Ta}_x\text{Nb}_x\text{O}_2$ oxides and the red points are c-HEOs); (d) XRD patterns of t-4 sample after heat treated at 1600 °C with different times (the inset is detailed XRD patterns at 27~32°); (e) CMAS infiltration depth of t-4 sample at 1300 °C for different corrosion times.

Fracture toughening behavior. Fracture toughness of the $\text{Zr}_{1-4x}\text{Y}_x\text{Yb}_x\text{Ta}_x\text{Nb}_x\text{O}_2$ oxides, along with other candidate top coat materials including c-HEOs, YSZ [30],

Gd₂Zr₂O₇ [31], 5Re₂Zr₂O₇ [12] and ReNbO₄ [32] is presented in Fig.3a. The state-of-the-art YSZ has a high fracture toughness of ~3.5 MPa m^{1/2} due to a ferroelastic toughening mechanism [1]. Other materials, such as *c*-HEOs, Gd₂Zr₂O₇, 5Re₂Zr₂O₇ and ReNbO₄, without any intrinsic toughening mechanism demonstrate a low fracture toughness. Among the Zr_{1-4x}Y_xYb_xTa_xNb_xO₂ oxides, the medium-entropy composition t-4 with double tetragonal phases shows the highest fracture toughness (~4.59 MPa m^{1/2}), which is even higher than YSZ. SEM observations on the indents (Fig.S5) show distinctly different fracture behaviors between the single-phase samples (t-2 and t-5) and two-phase samples (t-3 and t-4). For t-2 and t-5, cracks propagate through the grains, showing a transgranular fracture behavior. For most brittle ceramic materials, crack propagation corresponds to successive and repeated breaking of atomic bonds along specific crystallographic planes. On the contrary, for t-3 and t-4, cracks propagate mainly along the grain boundaries, showing an intergranular fracture behavior, which is a low-energy fracture mode. The tortuous crack deflections along the grain boundaries toughen the material and may contribute to a high fracture toughness.

To understand the improved fracture toughness of t-4, morphology of the grains adjacent to an indent is observed by SEM (Fig.3b), where twin domain switching can be observed, as pointed by the arrows in the figure. It should be pointed out that ferroelastic domain switching is only observed within a distance ~ 50 μm away from the center of the indent, indicating the ferroelastic transformation is stress-induced in both the t-ZrO₂(ABO₄) and T-ABO₄(ZrO₂). High magnification SE and BSE images (Fig.3c) show the presence of microcracks in the grains. These cracks can hardly propagate through grains due to the crack deflection caused by a variety of domain states. Atomic force microscope (AFM) analysis (Fig.3d) confirms these ~50 nm wide strip-like patterns arise from transformation of ferroelastic domains state. The ferroelastic domain switch around the indentation deflects crack direction and consequently raises the energy barrier for crack propagation, therefore cracks tend to propagate along grain boundaries with a lower energy barrier.

Bright field TEM micrograph in a <111> zone axis (Fig.3e) is utilized to determine

the crystallographic nature of each orthogonal domain or variant. The $\langle 111 \rangle$ selected area diffraction (SAD) patterns obtained from a grain with Zr-enriched t phase adjacent to the indent crack are shown in Fig.3f. The unique $\{112\}$ superlattice reflections are used to identify the number of ferroelastic twin variants. The presence of all three nonparallel $\{112\}$ superlattice reflections (the bottom SAD pattern in Fig.3f) reveals that the area “g” (Fig.3e) has undergone ferroelastic reorientation to form three orthogonal twin variants in response to the varying stress fields, whereas only a single variant (the upper SAD pattern in Fig.3f) is found in the matrix away from the crack. Bright field image of the ferroelastic domain process zone (Fig.3g) reveals patterns of nanoscale twin domains corresponding to the three tetragonal orientations. Two tetragonal domains are observed in the T- $\text{ABO}_4(\text{ZrO}_2)$ phase (Fig.S6), demonstrating that the ferroelastic domain transformation of tetragonal $\text{ABO}_4(\text{ZrO}_2)$ could also be stress-induced.

The coercive strain (γ^T) derived from ferroelasticity is directly related to the tetragonality (c/a) by $\gamma^T = (2/3)(c/a - 1)$ [33]. The tetragonality of the single t phase ($c/a \approx 1.026$) is higher than that of the T phase ($c/a \approx 1.022$), which indicates that the t phase is more prone to the stress-induced domain switch. No monoclinic phase is found in this grain away from the indent, indicating that the stress-induced ferroelastic deformation precedes the martensitic transformation at low stresses due to the sufficiently low effective critical shear stress for domain (twin) wall motion [34]. All the above observations demonstrate that ferroelastic domain transformation can be retained both for t and T phase to provide sufficient fracture toughness even without phase toughening at high temperature for TBCs application.

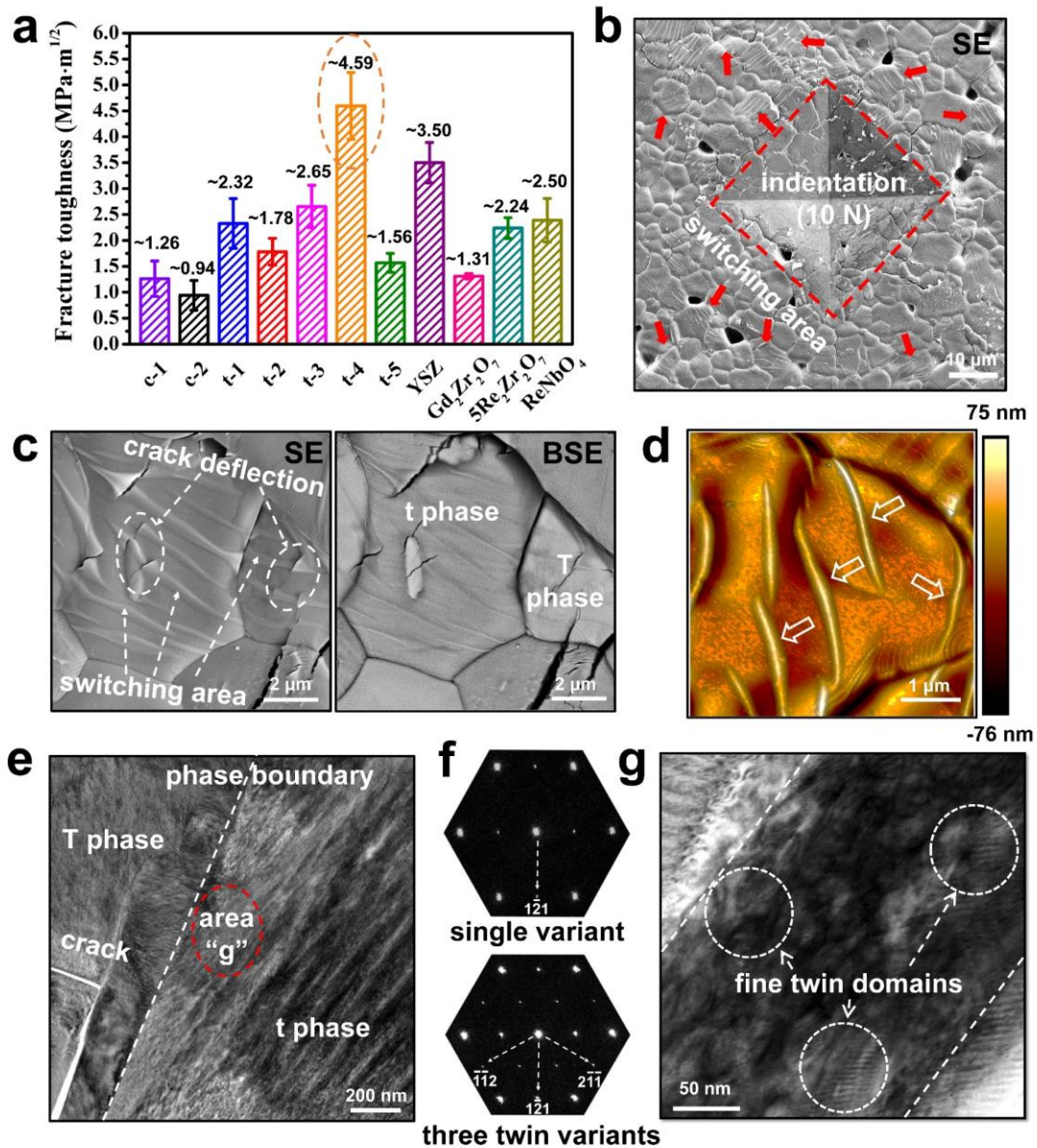


Figure. 3 | Ferroelastic toughening. (a) Fracture toughness of $Zr_{1-4x}Y_xYb_xTa_xNb_xO_2$ oxides; (b) SE images of indentation (10 N) imprint on the cross-section of thermal etched t-4 sample; (c) SE and BSE images of enlarged domain switching area of t- $ZrO_2(ABO_4)$ and T- $ABO_4(ZrO_2)$; (d) Ferroelastic domain switching observed by AFM; (e) Bright field TEM image along $[111]_{ZAP}$ of t-4 sample around an indentation crack; (f) The $[111]_{ZAP}$ SAD patterns of the t- $ZrO_2(ABO_4)$ matrix phase and ferroelastic domain process zone (the bottom SAD pattern corresponding to the regions “g” in the figure e); (g) Bright field TEM image of the ferroelastic domain process zone corresponding to the regions “g” in the figure e.

Besides the above discussed ferroelastic toughening, phase transformation observed in t-4 further increases the fracture toughness. Transformation of tetragonal to monoclinic phase is evident from the Raman spectrum collected from a crack tip (Fig.S7). The Raman peak at $\sim 182\text{ cm}^{-1}$ of monoclinic ZrO_2 phase is detected without presence of monoclinic ABO_4 , indicating that the t-m phase transformation only occurs in the t- $\text{ZrO}_2(\text{ABO}_4)$ solid solution.

Large numbers of deformation twins induced by the phase transformation are found along an intragranular crack (Fig.4a). Twinning deformations significantly consume the propagation energy of intergranular cracks and deflected them to the grain boundary with lower propagation energy. For example, as shown in Fig.4a, deformation of Twin 1 nucleates branch crack due to the lattice rotation at the twin boundary and large twinning shear at the twin tip. This consumes the propagation energy of the main crack. The multiple twins observed between Twin 2 and Twin 3 reveal discontinuous crack propagation where nucleation of twins consumes the stored energies at the crack front and impedes its growth. The crack is eventually directed towards the grain boundary along the shear direction of Twin 3.

All the above-mentioned twinning deformations take place in the Zr-enriched t- $\text{ZrO}_2(\text{ABO}_4)$ phase with a cation composition of $\text{Zr}_{0.737}\text{Y}_{0.048}\text{Yb}_{0.048}\text{Ta}_{0.066}\text{Nb}_{0.101}$ according to the EDS mapping results (Fig.4b). The $\langle 111 \rangle$ SAD patterns obtained from the Twin 2 area and the matrix material (inset figure in Fig.4d) confirm the presence of the monoclinic $\text{ZrO}_2(\text{ABO}_4)$ phase, suggesting the martensitic t \rightarrow m transformation could be stress-induced, even though the t- $\text{ZrO}_2(\text{ABO}_4)$ phase is retained at room temperature by increasing the configurational entropy using chemical doping. Notably, the t \rightarrow m martensitic transformation of t- $\text{ZrO}_2(\text{ABO}_4)$ results in a much lower dilatation strain than that of pure t- ZrO_2 with about 4-6% dilatation due to its smaller monoclinic angle ($\beta \approx 95.5^\circ$ for m- YTao_4).

The role of deformation twinning is twofold. It alleviates the stress concentrations at the crack front and toughens the material while it also impedes dislocation motion and improves the strength of the material. Two types of twin boundary are observed:

coherent twin boundary (CTB) of the Twin 1 (Fig.4c) and incoherent twin boundary (ICTB) of the Twin 2 (Fig.4e). The lattice rotation associated with deformation Twin 1 is $\sim 20^\circ$ and the interplanar spacing becomes much smaller (~ 0.251 nm) when the (101) lattice plane of tetragonal phase transforms to (002) of monoclinic phase, leading to the nucleation of branch crack (Fig.4a) by the grouping of dislocations pile-up against the CTB. The HAADF STEM image (Fig.4d) shows large amount of precipitates T- ABO_4 within a t- $\text{ZrO}_2(\text{ABO}_4)$ matrix near Twin 2. The nanocrystalline structure of tetragonal precipitates within matrix could bring in short diffusion distances and short circuit paths for solute redistribution resembling to the 8YSZ [35] and ZYTO [36]. Solute atoms (Y, Yb, Ta or Nd) in the t- $\text{ZrO}_2(\text{ABO}_4)$ solid solution are segregated along the incoherent twin boundary of Twin 2 so that the lattice distortions arising from the atomic size mismatch further emitted dislocations and exhausted the propagation energy of branch crack.

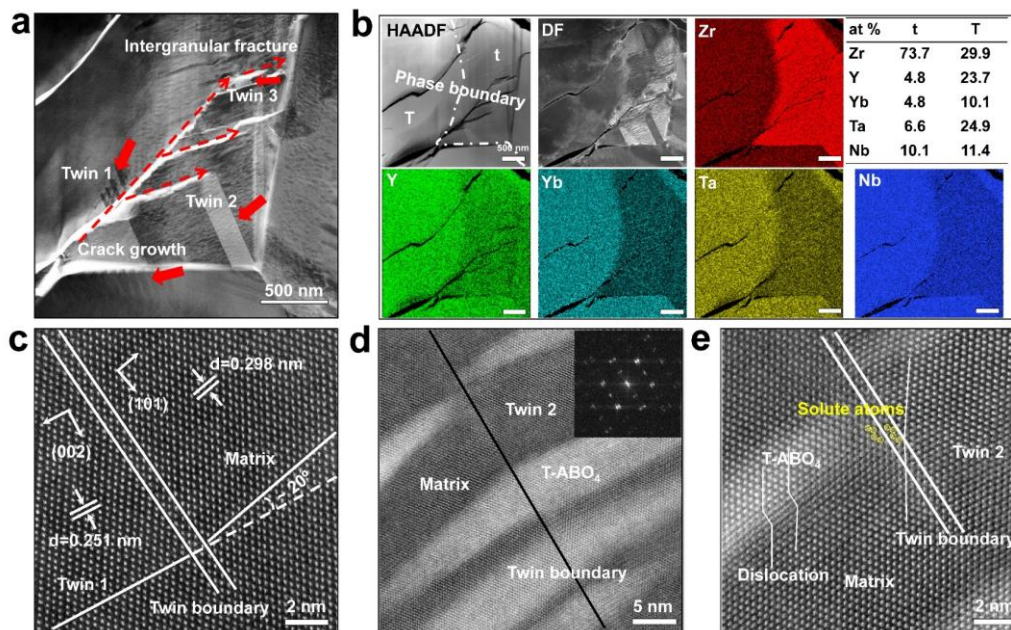


Figure. 4 | Twining deformations. (a) Bright-field STEM image showing the crack growth path of intragranular fracture; (b) HAADF, Dark-field STEM images and EDS maps of phase transformation area; (c) and (d) Atomic-resolution HAADF STEM images showing the structure of twinning boundary of Twin 1 and 2 taken along [111] zone axis in the figure a (the insert is $\langle 111 \rangle$ SAD patterns); (e) Enlarged atomic-resolution HAADF STEM images of Twin 2 area in the figure d.

3. Discussion

In summary, high-entropy principle was applied to stabilize the high-temperature tetragonal phase and successfully fabricated multicomponent medium- and high-entropy $Zr_{1-4x}Y_xYb_xTa_xNb_xO_2$ tetragonal oxides. Stress-induced ferroelastic domain variants and twinning transformation arising from the martensitic phase transformations should be responsible to the enhanced fracture toughness ($\sim 4.59 \text{ MPa m}^{1/2}$) of medium-entropy composition with double tetragonal phase. Meanwhile, ultrahigh CTE ($\sim 11.3 \times 10^{-6} \text{ K}^{-1}$ at $1000 \text{ }^\circ\text{C}$) was also achieved in this medium entropy composition. Competitive temperature-independent low thermal conductivities ($\sim 1.37 \text{ W}\cdot\text{m}^{-1}\cdot\text{K}^{-1}$ at $900 \text{ }^\circ\text{C}$) were obtained in the multicomponent $Zr_{1-4x}Y_xYb_xTa_xNb_xO_2$ as result of the enhanced phonon scattering rate arise from higher mass disorder and shorter phonon mean free path. Besides, excellent high-temperature thermal stability at $1600 \text{ }^\circ\text{C}$ and superior CMAS resistance ($\sim 2.9 \mu\text{m h}^{-1}$ at $1300 \text{ }^\circ\text{C}$) manifest that the multicomponent medium-entropy oxides reach a better balance in the overall properties than the high-entropy compositions for TBC application. The present work provides a novel route to design TBC materials by extending the high-entropy concept to both medium-entropy and high-entropy compositions for improved properties, especially when medium-entropy ceramics precede their high-entropy counterparts.

Acknowledgments

The authors thank National Natural Science Foundation of China (No. 51971139 and 51875341) and National Science and Technology Major Project of China (2017-VI-0011-0083) for funding.

References

- [1] N.P. Padture, M. Gell, E.H. Jordan, *Science*. 296 (2002) 280-284.
- [2] J. H. Perepezko, *Science* 326 (5956) (2009) 1068-1069.
- [3] D. R. Clarke, C. G. Levi, *Annu. Rev. Mater. Sci.* 33 (33) (2003) 383-417.
- [4] J. Chevalier, L. Gremillard, A.V. Virkar, D.R. Clarke, *J. Am. Ceram. Soc.* 92 (2009) 1901-1920.
- [5] D.R. Clarke, M. Oechsner, N.P. Padture, *MRS. Bull.* 37 (2012) 891-898.
- [6] X.Q. Cao, R. Vassen, W. Jungen, S. Schwartz, F. Tietz, D. Stöver, *J. Am. Ceram. Soc.* 84 (9) (2010) 2086-2090.
- [7] D. Zhu, D.S. Fox, N.P. Bansal, R.A. Miller, *NASA Briefs*, 2004.
- [8] R. Vaßen, M.O. Jarligo, T. Steinke, E.M. Daniel, S. Detlev, *Surf. Coat. Technol.* 205 (2010) 938-942.
- [9] C.M. Rost, E. Sachet, T. Borman, A. Moballeggh, E.C. Dickey, D. Hou, J.L. Jones, S. Curtarolo, J.P. Maria, *Nat. Commun.* 6 (2015) 8485.
- [10] Y. Sharma, B.L. Musico, X. Gao, C.Y. Hua, A.F. May, A. Herklotz, A. Rastogi, D. Mandrus, J.Q. Yan, H.N. Lee, M.F. Chisholm, V. Keppens, T.Z. Ward, *Phys. Rev. Mater.* 2 (2018) 060404.
- [11] J. Lu, Y. Chen, H. Zhang, N. Ni, L. Li, L. He, R. Mu, X. Zhao, F. Guo, *Cor. Sci.* 166 (2020) 108426.
- [12] K. Ren, Q. Wang, G. Shao, X. Zhao, Y. Wang, *Scr. Mater.* 178 (2020) 382-386.
- [13] Y. Shen, R.M. Leckie, C.G. Levi, D.R. Clarke, *Acta. Mater.* 58 (2010) 4424-4431.
- [14] S. Shian, P Sarin, M Gurak, M Baram, W.M. Kriven, D.R. Clarke, *Acta. Mater.* 69 (2014) 196-202.
- [15] C.A. Macauley, A.N. Fernandez, C.G. Levi, *J. Eur. Ceram. Soc.* 37 (2017) 4888-4901.
- [16] J. Gild, M. Samiee, J.L. Braun, T. Harrington, H. Vega, P.E. Hopkins, K. Vecchio, J. Luo, *J. Eur. Ceram. Soc.* 38 (2018) 3578-3584.
- [17] A. Sarkar, B. Breitung, H. Hahn, *Scr. Mater.* 187 (2020) 43-48.
- [18] A.J. Wright, J. Luo, *J. Mater. Sci.* 55 (23) (2020) 1-16.

- [19] M. Gurak, Q. Flamant, L. Laversenne, D.R. Clarke, *J. Eur. Ceram. Soc.* 38 (2018) 3317-3324.
- [20] G. Anand, A.P. Wynn, C.M. Handley, C.L. Freeman, *Acta Mater.* 146 (2018) 119–125.
- [21] D.J. Kim, T.Y. Tien, *J. Am. Ceram. Soc.* 74 (1991) 3061-3065.
- [22] F. Wang, X. Zhang, X. Yan, Y. Lu, M. Nastasi, Y. Chen, B. Cui, *J. Am. Ceram. Soc.* 103 (8) (2020) 4463-4472.
- [23] S.A. Matcher, P.K. Davies, *J. Am. Ceram. Soc.* 78 (10) (1995) 2737-2745.
- [24] M.J. Maloney, US patent. 2000.
- [25] P. K. Schelling, S. R. Phillpot, R. W. Grimes, *Phil. Mag. Lett.* 84 (2) (2004) 127-137.
- [26] Q. U. Zhixue, C. Wan, W. Pan, *Acta Mater.* 60 (6-7) (2012) 2939-2949.
- [27] L. Chen, M. Hu, P. Wu, J. Feng, *J. Am. Ceram. Soc.* 102 (8) (2019) 4809-4821.
- [28] S.C. Jiang, T. Hu, J. Gild, N.X. Zhou, J.Y. Nie, M.D. Qin, T. Harrington, K. Vecchio, J. Luo, *Scr. Mater.* 142 (2018) 116-120.
- [29] D. Wu, H. Zhang, X. Shan, F. Yang, F. Guo, X. Zhao, P. Xiao, S. Gong, *J. Am. Ceram. Soc.* 103 (5) (2020) 3401-3415.
- [30] R. Vassen, X. Cao, F. Tietz, D. Basu, D. Stöver, *J. Am. Ceram. Soc.* 83 (8) (2000) 2023–2028 .
- [31] Y. Zhang, L. Guo, X. Zhao, C. Wang, F. Ye, *Mater. Sci. Eng. A* 648 (2015) 385-391.
- [32] P. Zhang, Y. Feng, Y. Li, W. Pan, P. Zong, M. Huang. Y. Han, Z. Yang, H. Chen, Q. Gong, C. Wan, *Scr. Mater.* 180 (2020) 51-56.
- [33] C. Mercer, J.R. Williams, D.R. Clarke, A.G Evans, *Proc. Roy. Soc.* 463 (2007) 1393-1408.
- [34] F.R. Chien, F.J. Uvic, V. Prakash, *Acta Mater.* 46 (6) (1998) 2151-2171.
- [35] J.A. Krogstad, R.M. Leckie, S. Krämer, J.M. Cairney, D.M. Lipkin, C.A. Johnson, C.G. Levi, *J. Am. Ceram. Soc.* 96 (2013) 299–307.
- [36] J.S. Van Sluytman, S Krämer, V.K. Tolpygo, C.G. Levi, *Acta. Mater.* 96 (2015)

133-142.

Figures

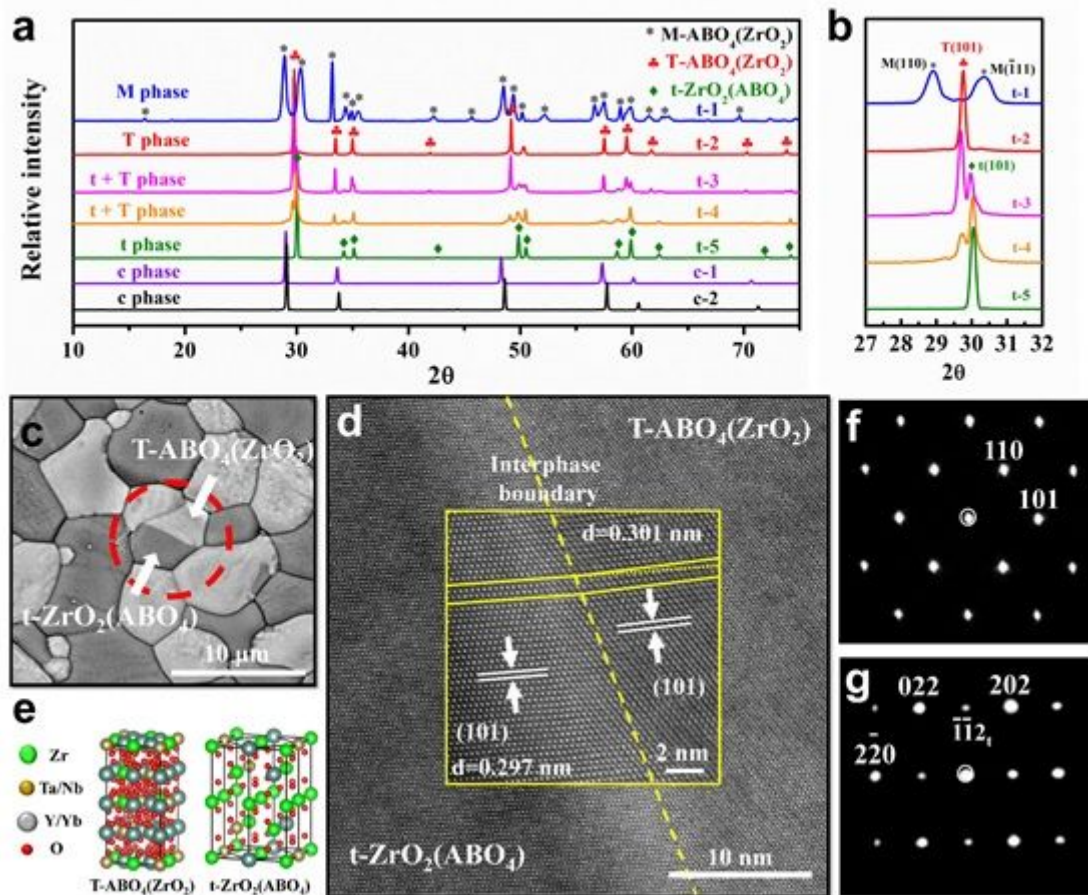


Figure 1

Phase identification. (a) XRD patterns of $\text{Zr}_{1-4x}\text{Y}_x\text{Y}_b\text{xTa}_x\text{Nb}_x\text{O}_2$ oxides and cubic phase HEOs (site A in the crystal structure ABO_4 represents Y or Yb, and site B represents Ta or Nb); (b) Slow scan (0.50 min^{-1}) of the 2θ range between 27° and 32° to distinguish the monoclinic and tetragonal phase; (c) BSE image of the grain with the double tetragonal phases in the t-4 sample; (d) Atomic-resolution HAADF STEM image of the interphase boundary between the T- $\text{ABO}_4(\text{ZrO}_2)$ and t- $\text{ZrO}_2(\text{ABO}_4)$ phase (the inset figure is an expanded view of the interphase boundary); (e) Crystal structure of T- $\text{ABO}_4(\text{ZrO}_2)$ and t- $\text{ZrO}_2(\text{ABO}_4)$ created using VESTA software package; (f) The $[1(-)11]$ ZAP of T- $\text{ABO}_4(\text{ZrO}_2)$ and (g) the $[111]$ ZAP of t- $\text{ZrO}_2(\text{ABO}_4)$.

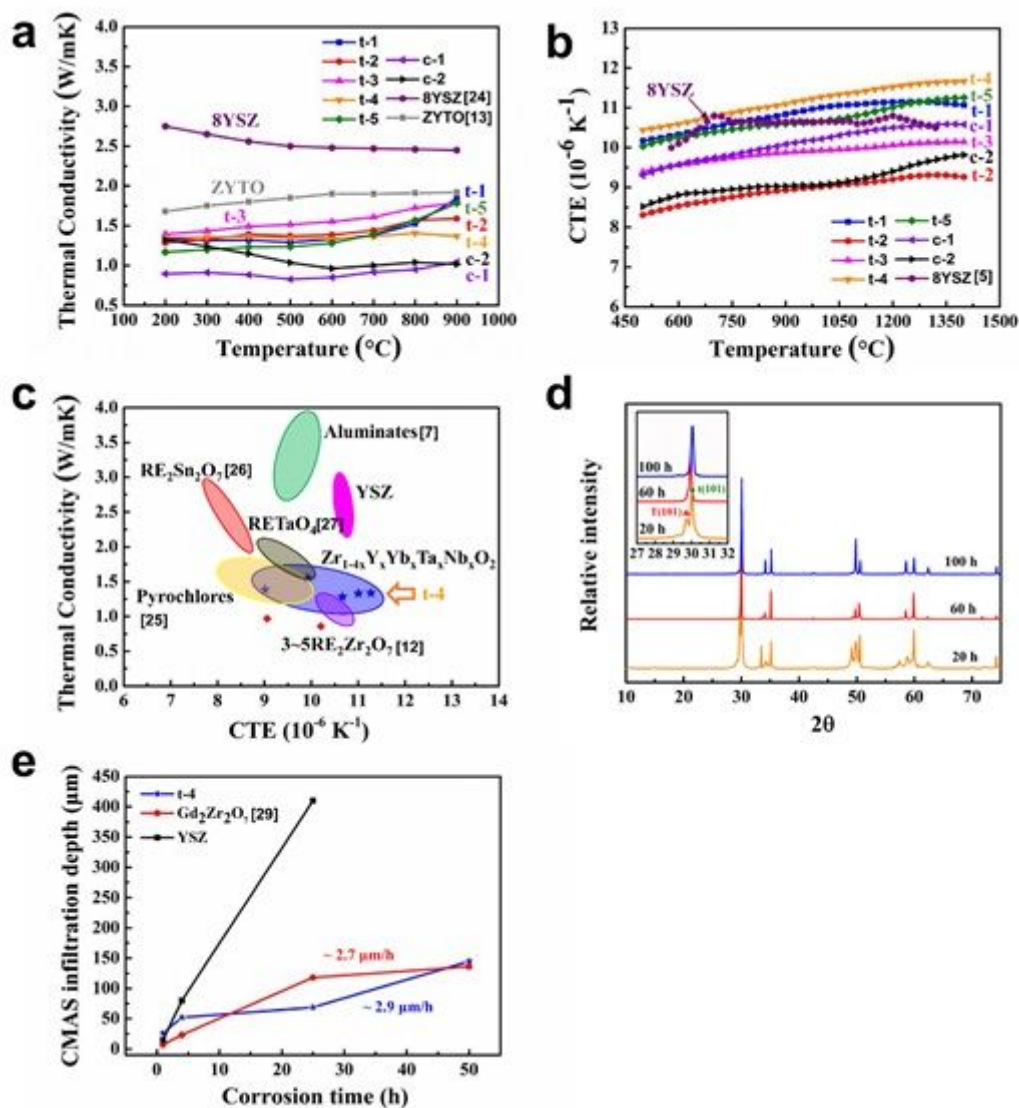


Figure 2

Thermal properties and CMAS resistance. (a) Thermal conductivity of Zr₁₋₄xY_xY_bTa_xNb_xO₂ oxides, compared with YSZ and ZYTO; (b) Thermal expansion coefficient of Zr₁₋₄xY_xY_bTa_xNb_xO₂ oxides, compared with YSZ; (c) Thermal conductivity as a function of thermal expansion coefficient (the blue points are data of Zr₁₋₄xY_xY_bTa_xNb_xO₂ oxides and the red points are c-HEOs); (d) XRD patterns of t-4 sample after heat treated at 1600 °C with different times (the inset is detailed XRD patterns at 27~32°); (e) CMAS infiltration depth of t-4 sample at 1300 °C for different corrosion times.

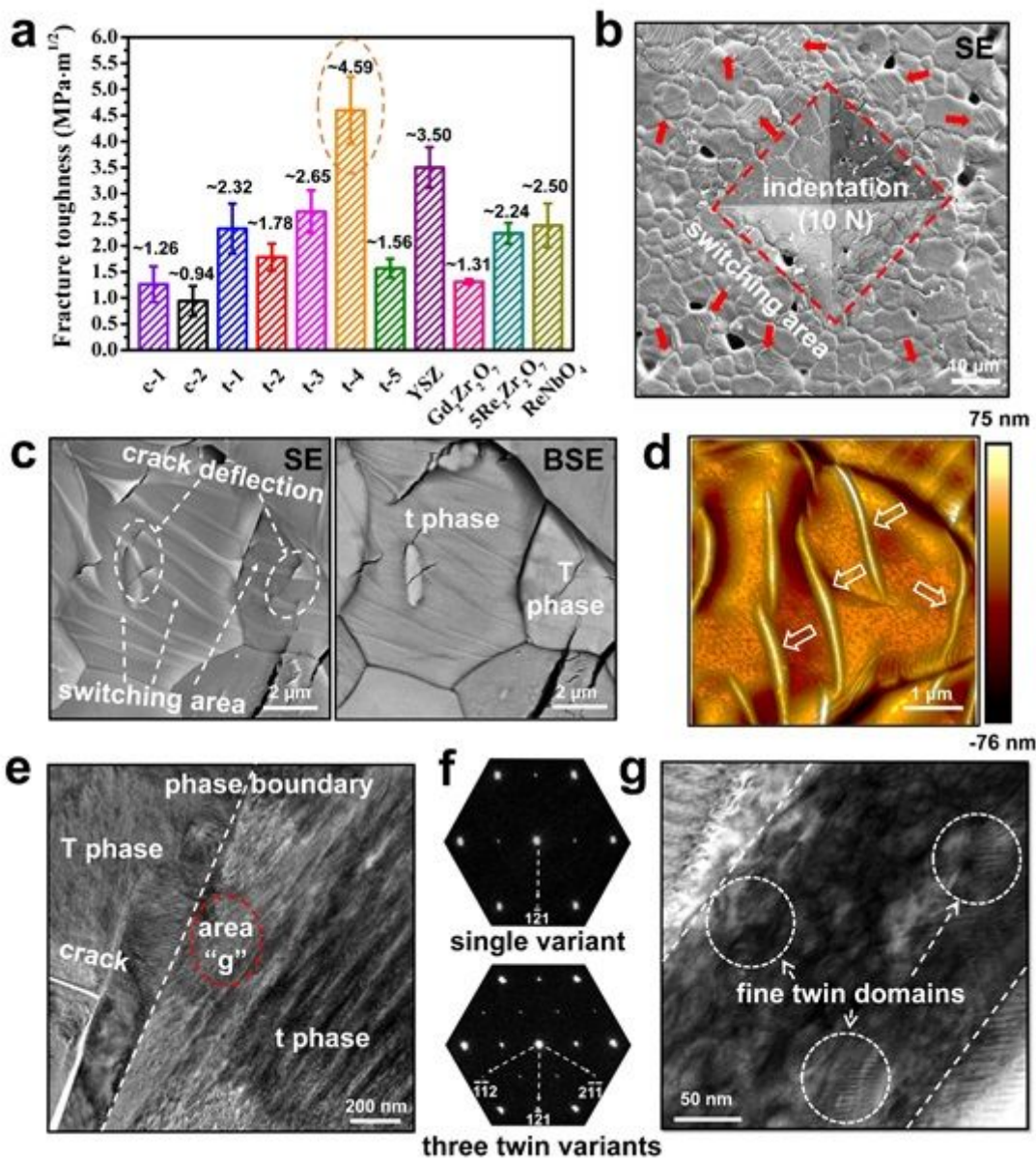


Figure 3

Ferroelastic toughening. (a) Fracture toughness of $Zr_{1-4x}Y_xY_{bx}Ta_xNb_xO_2$ oxides; (b) SE images of indentation (10 N) imprint on the cross-section of thermal etched t-4 sample; (c) SE and BSE images of enlarged domain switching area of t-ZrO₂(ABO₄) and T-ABO₄(ZrO₂); (d) Ferroelastic domain switching observed by AFM; (e) Bright field TEM image along [111]ZAP of t-4 sample around an indentation crack; (f) The [111]ZAP SAD patterns of the t-ZrO₂(ABO₄) matrix phase and ferroelastic domain process zone (the bottom SAD pattern corresponding to the regions "g" in the figure e); (g) Bright field TEM image of the ferroelastic domain process zone corresponding to the regions "g" in the figure e.

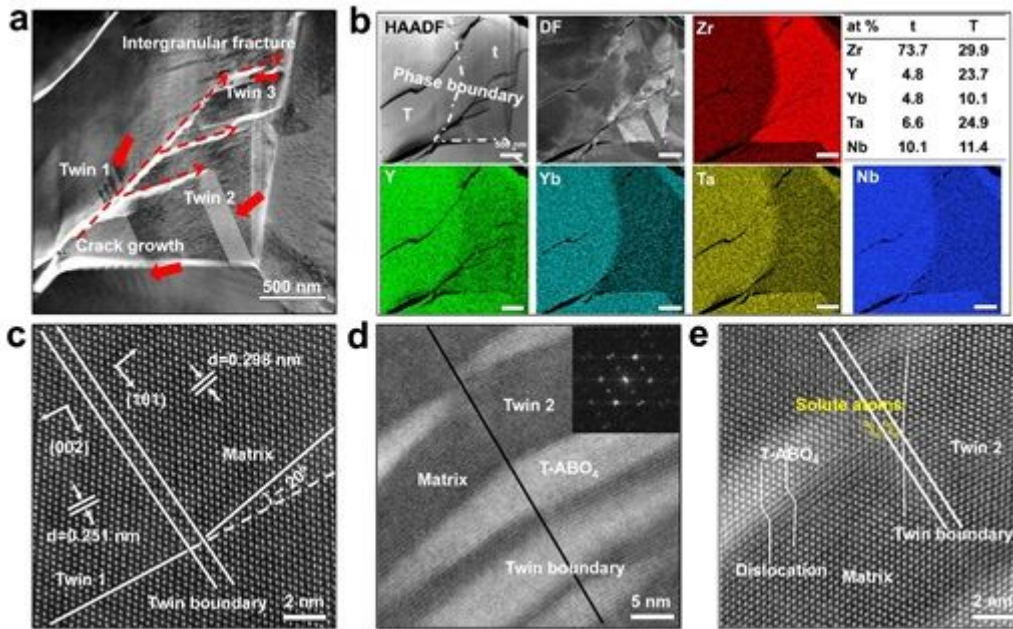


Figure 4

Twining deformations. (a) Bright-field STEM image showing the crack growth path of intragranular fracture; (b) HAADF, Dark-field STEM images and EDS maps of phase transformation area; (c) and (d) Atomic-resolution HAADF STEM images showing the structure of twinning boundary of Twin 1 and 2 taken along $[111]$ zone axis in the figure a (the insert is $\langle 111 \rangle$ SAD patterns); (e) Enlarged atomic-resolution HAADF STEM images of Twin 2 area in the figure d.

Supplementary Files

This is a list of supplementary files associated with this preprint. Click to download.

- [Supplementinformation.docx](#)